1   **Retrieval Algorithm for Aerosol Effective Height from the**

2   **Geostationary Environment Monitoring Spectrometer (GEMS)**

3

4   Sang Seo Park[1,*], Jhoon Kim[2], Yeseul Cho[2], Hanlim Lee[3], Junsung Park[3], Dong-Won

5   Lee[4], Won-Jin Lee[4], Deok-Rae Kim[4]

6   *[1] Department of Urban and Environmental Engineering, Ulsan National Institute of Science*

7   *and Technology, Ulsan, Korea*

8   *[2]Department of Atmospheric Sciences, Yonsei University, Seoul, Korea*

9   *[3]Division of Earth and Environmental System Sciences, Pukyong National University, Busan,*

10   *South Korea*

11   *[4]Envionment Satellite Center, National Institute of Environmental Research, Incheon, Korea*

12

13

14

15   *Corresponding author. Sang Seo Park (sangseopark@unist.ac.kr)

16

17

18   Submitted to Atmospheric Measurement Techniques

19   2023. 06.

20

21

22   **Abstract**

23   An algorithm for aerosol effective height (AEH) was developed for operational use

24   with observations from the Geostationary Environment Monitoring Spectrometer

25   (GEMS). The retrieval technique uses the slant column density of the oxygen dimer

26   (O_2-O_2) at 477 nm, which is converted into AEH after retrieval of aerosol and surface

27   optical properties from GEMS operational algorithms. The AEH retrieval results show

28   significant AEH values and continuously monitor aerosol vertical height information in

29   severe dust plumes over East Asia, and the collection of plume height information for

30   anthropogenic aerosol pollutants over India. Compared to the AEH retrieved from

31   Cloud-Aerosol Lidar with Orthogonal Polarization (CALIOP), the retrieval results show

32   insignificant bias with a standard deviation of 1.4 km for the AEH difference over the

33   GEMS observation domain from January to June 2021 due to uncertainty in input

34   parameters for aerosol and surface. The AEH difference depends on aerosol optical

35   properties and surface albedo. Compared to the aerosol layer height obtained from the

36   tropospheric monitoring instrument (TROPOMI), differences of 0.78 ± 0.81 and $1.16 \pm$

37   0.92 km were obtained for pixels with single scattering albedo (SSA) < 0.90 and $0.90 <$

38   SSA < 0.95, respectively, with significant dependence on aerosol type.

39

40   Keywords: aerosol effective height, aerosol optical depth, environmental satellite,

41   GEMS

42

43

1. Introduction

44

45 Since the launch of the Total Ozone Mapping Spectrometer (TOMS) on Nimbus-7,

46 ultraviolet (UV)-visible satellite measurements have been used for environmental

47 monitoring of the distribution and reaction processes of pollutants (e.g., anthropogenic

48 aerosols, tropospheric ozone, NO_2, and SO_2). Measurements from environmental

49 satellites have been used to estimate gaseous species in the atmosphere, resulting in

50 vertical column integrated amounts. However, these column-integrated amounts and

51 associated surface concentrations have uncertainty due to simultaneous changes in

52 optical path length associated with the vertical distribution of target species and

53 amounts of scattering materials (clouds and aerosols) present. For this reason,

54 environmental satellite sensors, in particular those that measure UV-visible wavelength

55 range, have been used to retrieve aerosol and cloud signals to determine aerosol index

56 (e.g., Buchard *et al.*, 2015; Herman *et al.*, 1997; Torres *et al.*, 1998, 2002; Prospero *et*

57 *al.*, 2000; de Graaf *et al.*, 2005) and scattering radiative index values (Penning de Vries

58 *et al.*, 2009, 2015; Kooreman *et al.*, 2020; Kim *et al.*, 2018). In addition, measurements

59 of scattering material amounts, such as aerosol optical depth (AOD) in UV wavelengths

60 and radiative cloud fraction amounts, have also been retrieved from pixel-based

61 radiance data. Although the algorithms developed for environmental satellite sensors

62 indicate the presence and amount of scattering materials, the accuracy of these retrieval

63 algorithms for trace gases is significantly affected by the relative vertical distributions

64 between trace gases and scattering materials (e.g., Lorente *et al.*, 2017; Hong *et al.*,

65 2017). For this reason, estimating cloud and aerosol vertical parameters is very

66 important.

67 For cloud vertical information, cloud height information has been estimated

Atmospheric
Measurement
Techniques
Discussions

Open Access

EGU

68   simultaneously with cloud optical depth and radiative cloud fraction data using the

69   rotational Raman scattering (Joiner and Vasilkov, 2006; Vasilkov *et al.*, 2008; Joiner and

70   Bhartia, 1995) and absorption intensity of the oxygen dimer (O_2-O_2) (Accarreta *et al.*,

71   2004; Vasilkov *et al.*, 2018; Choi *et al.*, 2021) combined with normalized radiance.

72   Because cloud optical properties are relatively simple and cloud optical depth is thick,

73   vertical information of cloud can be accurately determined. Similarly, the aerosol

74   vertical distribution can be estimated using the oxygen-related absorption bands, such as

75   the O_2-O_2 (Park *et al.*, 2016; Chimot *et al.*, 2017; Choi *et al.*, 2019, 2020), O_2-A

76   (Dubisson *et al.*, 2009; Geddes and Boesch, 2015; Sanders *et al.*, 2015; Zeng *et al.*,

77   2020), and O_2-B (Chen *et al.*, 2021; Ding *et al.*, 2016) bands, as well as combinations of

78   these bands (Sanghavi *et al.*, 2012). However, the vertical distribution of aerosol is more

79   difficult to assess than that of clouds, as the optical properties of aerosols in the

80   atmosphere differ among aerosol types.

81   Recently, various aerosol retrieval algorithms have been developed for use with

82   satellite sensors. These algorithms focus on improved trace gas retrieval as well as

83   direct monitoring of aerosol properties. For this reason, AOD and other aerosol optical

84   properties, such as single scattering albedo (SSA), are retrieved from the observed

85   radiance (e.g., Ahn *et al.*, 2014; Kim *et al.*, 2020; Torres et al., 2020). In addition, an

86   algorithm for aerosol vertical information has been developed based on hyperspectral

87   UV-visible radiance from satellite observation. Nanda *et al.* (2018) demonstrated the

88   possibility of aerosol height retrieval from the O_2-A band developed an algorithm using

89   Tropospheric Monitoring Instrument (TROPOMI) (Sanders and de Haan, 2016; Nanda

90   *et al.*, 2020).

91   The Geostationary Environment Monitoring Spectrometer (GEMS), which was

Atmospheric
Measurement
Techniques
Discussions

Open Access
EGU

92   launched by South Korea in February 2020, retrieves data related to major trace gases

93   and aerosol properties (Kim *et al.*, 2020). Aerosol properties are obtained for the

94   purposes of monitoring surface air quality and aerosol effects for the air mass factor

95   (AMF) calculation. In addition to the aerosol optical property algorithm, the standard

96   product of aerosol is additionally applied to the aerosol vertical information, aerosol

97   effective height (AEH).

98   For the possibility for development of an AEH retrieval algorithm, Park *et al.* (2016)

99   conducted theoretical sensitivity testing of AEH retrieval using solely the O_2-O_2

100   absorption band along with aerosol and surface properties. Overall, the sensitivity of

101   AEH retrieval was strongly affected by SSA, AOD, and aerosol types including optical

102   and size properties, and the error budget for AEH retrieval using the O_2-O_2 band was

103   739 ~ 1276 m. In addition, case studies of AEH during dust transport over East Asia

104   were conducted using radiance data from the Ozone Monitoring Instrument (OMI) and

105   aerosol optical properties from the Moderate Resolution Imaging Spectroradiometer

106   (MODIS).

107   Based on theoretical considerations and case results of previous studies, we introduce

108   an operational retrieval algorithm for AEH. Section 2 describes the details of the AEH

109   retrieval algorithm for GEMS and provides a list of the detailed input parameters.

110   Section 3 introduces the details of satellite sensors for the comparison and validation in

111   this study. Section 4 reports retrieval results based on case studies of aerosol transport,

112   and section 5 contains validation results based on Cloud-Aerosol Lidar with Orthogonal

113   Polarization (CALIOP) and TROPOMI data. Finally, we show conclusion and summary

114   in section 6.

115

2. AEH retrieval algorithm

116

117 AEH is a layer height parameter that considers the penetration of photons into the

118 aerosol layer. A detailed definition of AEH was introduced by Park *et al.* (2016).

119 Numerous previous studies have used the aerosol top layer height (Kohkanovsky and

120 Rozanov, 2010) or middle layer height (e.g., Sanders *et al.*, 2015; Nanda *et al.*, 2020) as

121 the aerosol vertical layer parameter, which represents the highest altitudes with existing

122 effective aerosol extinction sensitivity. However, the definition of AEH requires that the

123 altitude region for aerosol extinction be integrated from the surface to $(1-\exp^{-1}) \times$ AOD.

124 Therefore, AEH is similar to the aerosol top layer height but with a slight bias. For AEH

125 retrieval, the vertical distribution assumption is also important. The Gaussian Density

126 Fitting (GDF) distribution, which is a modified Gaussian distribution structure, is

127 assumed for AEH retrieval. The full-width at half-maximum (FWHM) of the aerosol

128 layer is 1 km. Based on the assumptions about the aerosol vertical distribution, the AEH

129 value is greater than the peak height of the Gaussian distribution and lower than the

130 aerosol top layer height.

Atmospheric
Measurement
Techniques
Discussions
Open Access
EGU
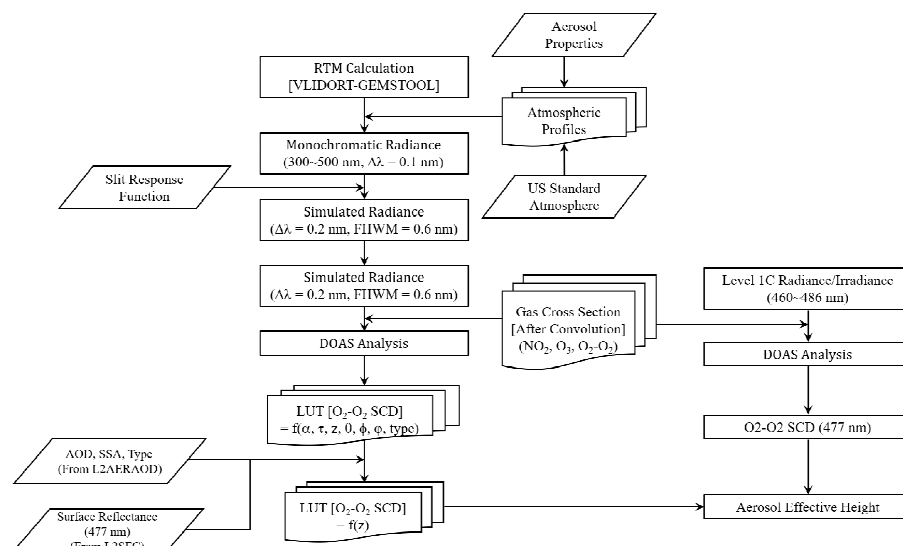
Figure 1. Flowchart of the AEH retrieval algorithm for GEMS satellite observation.

Figure 1 shows the overall flowchart of the AEH algorithm. Because the spectral coverage is limited to 300-500 nm, the AEH from GEMS is applied to the O_2-O_2 absorption band. In AEH estimation, other aerosol characteristics, including aerosol amounts and optical properties, affect retrieval accuracy. The main purpose of GEMS is to monitor air quality, and aerosol properties are targets of such monitoring over East Asia. For this reason, the GEMS aerosol algorithm was developed as multiple operational products. The GEMS Level 2 aerosol operational algorithm (L2AERAOD) retrieves the aerosol index (AI) values for UV and visible wavelengths, as well as AOD and SSA with considering the aerosol types (National Institute of Environmental Research, 2020a). Park *et al.* (2016) noted that the error budget of AEH is significantly affected by uncertainty in AOD and SSA and by the misclassification of aerosol types, which is directly related to the optical property and size information. Therefore, the

Atmospheric
Measurement
Techniques
Discussions

Open Access

EGU

146 L2AERAOD results for AOD and SSA at 550 nm were adopted as input data for aerosol

147 properties.

148 Although L2AERAOD retrieved their own surface reflectance for accurate separation

149 of surface signals from total reflectance at the top of the atmosphere (TOA), the

150 standard product for surface reflectance (L2SFC) (National Institute of Environmental

151 Research, 2020b) was also independently retrieved from long-term GEMS

152 radiance/irradiance data. L2SFC is the reference product for spectral surface reflectance.

153 To consider the various retrieval products, the L2SFC retrieves the surface reflectivity

154 in multiple spectral channels, and retrieves the black surface reflectivity (BSR) and bi-

155 directional reflectance distribution function (BRDF) based on the original pixel

156 resolution. Because observation geometries are limited by the geostationary satellite

157 position, surface properties related to the directional dependency have significant

158 uncertainty. However, L2SFC accurately retrieved surface optical properties with high

159 spatial resolution. For this reason, L2SFC was used as reference data for the surface

160 products for all trace gas retrieval algorithms. Similarly, the AEH retrieval algorithm

161 also uses L2SFC as a reference surface property. Specifically, the BSR value at 477 nm

162 is used as the surface reflectance input for AEH retrieval.

163 **Table 1.** Details of fitting parameter for O_2-O_2 SCD estimation via the DOAS method.

Parameter	
Fitting window	460 – 486 nm
Absorption cross section	NO_2 at 220 and 294 K (Vandaele *et al.*, 1998)
	O_3 at 223, 243 and 293K (Bogumil *et al.*, 2001)
	O_2-O_2 at 293 K (Thalman and Volkamer, 2013)
	Ring

164　　For AEH retrieval, the basic method is the identification of changes in optical path

165　　length caused by effective aerosol layer height variation. To measure the optical path

166　　length change, O_2-O_2 slant column density (SCD) retrieved by the differential optical

167　　absorption spectroscopy (DOAS) method was used. From Nanda *et al.* (2020),

168　　TROPOMI uses the O_2-A band for aerosol layer height (ALH) retrieval. In the GEMS

169　　product, however, the O_2-O_2 SCD at 477 nm absorption band is used because this

170　　absorption band is strongest absorption band within the GEMS spectral observation

171　　range. Detailed DOAS fitting parameter and setting information is provided in Table 1

172　　for the estimation of O_2-O_2 SCD from both the simulation and observation data. After

173　　the estimation of O_2-O_2 SCD, conversion from O_2-O_2 SCD to AEH is an essential

174　　process. For this conversion, a look-up table (LUT) approach between O_2-O_2 SCD and

175　　AEH was used with consideration of observation geometries, surface conditions, and

176　　aerosol optical properties.

177

178　　**Table 2.** Ratio between SCD error and the SCD of O_2-O_2 according to the polynomial

179　　order and offset settings used for DOAS fitting.

Polynomial	Offset = none	Offset = 0th
2nd order	6.06 ± 2.07	6.79 ± 2.31
3rd order	6.32 ± 2.20	6.79 ± 2.32
4th order	7.86 ± 2.78	7.34 ± 2.85

180

181　　Observed radiance fitting is affected by noise signals during radiance observation. To

182　　minimize the noise effect and improve fitting quality, the optimal settings for fitting

183   were also analyzed. Table 2 shows ratios of SCD error to the SCD for various

184   polynomial and bias orders from observed radiance. Although the fitting quality was

185   good overall, the setting with the smallest error was used in this study.

186   Table 3 shows the dimension of the LUT for the AEH retrieval algorithm. To

187   calculate the LUT, a linearized pseudo-spherical vector discrete ordinate radiative

188   transfer model (VLIDORT) version 2.6 was used (Spurr, 2013). After calculating

189   spectral radiance with 0.1 nm sampling, we performed the slit response function of

190   GEMS and sampling specification prior to the DOAS fitting. For O_2-O_2 absorption, the

191   absorption cross section used for the radiative transfer model calculation is considered

192   the temperature dependent absorption cross section (e.g., Park *et al.*, 2017). The O_2-O_2

193   SCD error is significantly reduced with the use of simulated radiance because the

194   simulated radiance is not considered to contain noise. By contrast, the observed radiance

195   has a signal to noise ratio (SNR) of approximately 1000. Therefore, the observed

196   radiance has greater fitting error than the those from the simulated radiance, although

197   the bias between observation and simulation results is not significant.

198   O_2-O_2 SCD decreases with increasing AEH for all aerosol types and AOD (Park *et al.*,

199   2016). In addition, the O_2-O_2 SCD sensitivity is enhanced at high AOD and absorbing

200   dominant aerosol cases. Radiation is mostly scattered from the top of the aerosol layer

201   for thick aerosols, and the effective scattering layer penetrates more deeply into the

202   layer when the aerosol layer is thinner. In addition, the contrast of O_2-O_2 is greater for

203   absorbing dominant aerosols than scattering dominant aerosols because the optical

204   reflection change per unit of layer depth change is large for absorbing aerosols. Based

205   on the changes in sensitivity observed for optical path length, aerosol type (in particular

206   in terms of SSA) and AOD are considered to significantly affect AEH retrieval.

207   **Table 3.** The dimension of the LUT for the GEMS AEH retrieval algorithm used to

208   estimate AEH from O_2-O_2 SCD. (SZA: solar zenith angle, VZA: viewing zenith angle,

209   RAA: relative azimuth angle, SUR: surface reflectance).

Variable [unit]	No. of entries	Entries	
Spectral range [nm]	-	455~491 nm (0.1 nm interval)	
SZA [º]	8	0.01,10, 20, 30, 40, 50, 60, 70	
VZA [º]	8	0.01, 10, 20, 30, 40, 50, 60, 70	
RAA [º]	10	0.01,20, 40, 60, 80, 100, 120, 140, 160, 180	
SUR	7	0.0, 0.02, 0.05, 0.1, 0.2, 0.3, 0.5	
AOD at 440 nm	9	0.04, 0.2, 0.5, 1.0, 1.5, 2.0, 2.5, 3.0, 5.0	
Refractive Index (Imaginary) at 440 nm	3×7	Absorbing	0.0, 0.00206, 0.00453, 0.00738, 0.01233, 0.018, 0.02436, 0.03136
		Dust	0.0, 0.00053, 0.00113, 0.00181, 0.00298, 0.00437, 0.00603, 0.00804
		Non-Absorbing	0.0, 0.00124, 0.00258, 0.00399, 0.00547, 0.0086, 0.01197, 0.01555
AEH [km]	10	0.2, 0.5, 1.0, 1.5, 2.0, 2.5, 3.0, 3.5, 4.0, 5.0	
Terrain Height [km]	2	0.0, 2.0	

210

211   **3. Data**

212   **3.1. TROPOMI**

213   The TROPOMI is spectrometer to observe the radiance from UV to near IR onboard

214   the Sentinel-5 Precursor (Sentinel-5P) satellite. The orbit for Sentinel-5P is a polar orbit

215   with ascending node crossing to equator at 13:30 local time. The aerosol layer height

216   product from TROPOMI (AER_LH) retrieves vertically localized aerosol layers in free

217   troposphere by using the level 1b earth radiance measurements from 758 to 770 nm (de

218   Graaf *et al.*, 2022). Spectral fit estimation of reflectance around the O_2-A band is based

219   on a neural network for the forward model calculation. After cloud masking to avoid the

220   cloud affected pixels, an optimal estimation method was used to retrieve the aerosol

221   layer height parameters for the inversion method. During the radiance fitting, AOD is

222   also used as the main fitting parameter, but other aerosol parameters, such as SSA and

223   scattering phase function, are assumed to be fixed values (Nanda et al., 2020). The

224   target requirement on the accuracy and precision is 0.5 km or 50 hPa, and the threshold

225   requirement is 1 km or 100 hPa (de Graaf et al., 2022). In this study, we use version

226   2.0.0 of the TROPOMI offline level 2 AER_LH product with the spatial resolution is

227   3.5 km × 7 km at nadir viewing geometry.

228

229   **3.2. CALIOP**

230   The CALIOP is a spaceborne lidar sensor onboard the Cloud-Aerosol Lidar and

231   Infrared Pathfinder Satellite Observations (CALIPSO) to measure the vertical

232   information of aerosol and cloud with estimating the optical properties. The CALIOP

233   has two different wavelength channels (532 and 1064 nm) by using the Nd:YAG laser to

234   generate the signals (Winker et al., 2009). This sensor is Sun synchronous orbit

235   constelled to the A-train, and also cross to equator at 13:30 local time by ascending

236   node. For the vertical information, the resolution for vertical sampling is 30 m below 8

237   km altitude, and 60 m from 8 to 20 km altitude, respectively. Although the pixel data

238   can retrieve with extremely high horizontal and vertical resolutions, the spatial coverage

239   is narrow. In this study, the data of Level 2 aerosol profile product (version 3.41) was

240   used. Because the aerosol profile product exists the vertical distribution of aerosol

Atmospheric
Measurement
Techniques

Discussions

Open Access

EGU

241   extinction coefficient, representative layer height parameter is estimated by using the

242   vertical profile of extinction coefficient at 532 nm.

243

244   **4. Case studies**

245   Figure 2 shows retrieval results for AEH, AOD, and SSA from GEMS on March 29

246   over East Asia. Because the operational schedule is hourly during the daytime, the

247   GEMS retrieval results are shown at 1-hour intervals from 01:00 to 07:00 Universal

248   Time Coordinated (UTC). Based on the retrieval sensitivity of AEH, only AEH retrieval

249   results with AOD greater than 0.3 are shown. During this case study, a Yellow dust

250   plume was located along the coast of China and South Korea with AOD at 443 nm of

251   0.8~1.2. Simultaneously, another plume was also present over the northeastern Korean

252   Peninsula with AOD of 1.0~2.0 at 443 nm. SSA at 443 nm was 0.90~0.93 for the plume

253   over South Korea and 0.87~0.90 for the plume over the northeastern Korean Peninsula.

254   Although the AOD and SSA for these plumes are differed significantly, their AEH

255   results were similar. For both plumes, AEH shows around 1.0~2.0 km in this case. In

256   addition, the retrieved AEH values exhibited insignificant diurnal variation in regions

257   with severe dust plumes.

258
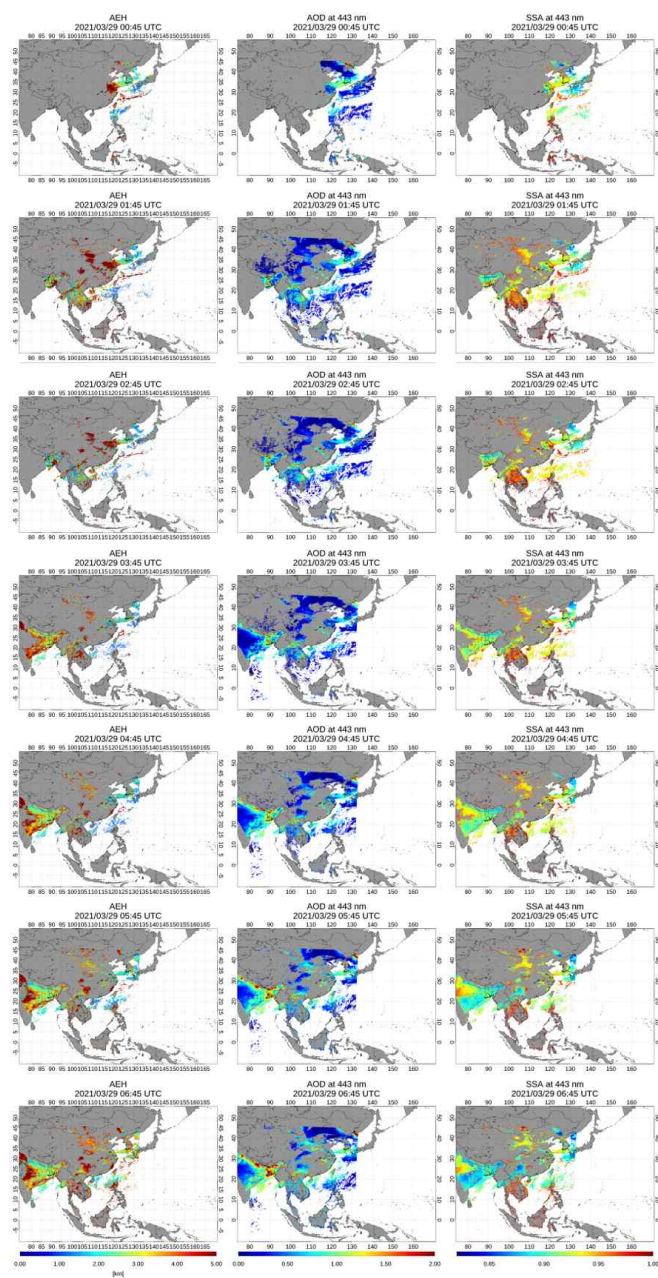
Figure 2. Case study results for AEH, AOD, and SSA based on GEMS observations

on March 29, 2021.

261   As shown in Figure 2, an additional severe aerosol plume was present over

262   northeastern India, with AOD at 443 nm of 1.0~2.0 and SSA at 443 nm of 0.85~0.90.

263   From Rana *et al.* (2019), metropolitan cities and industrial cluster in India are heavy

264   emitters of black carbon, and high concentrations of black carbon are distributed over

265   the Indo-Gangetic Plain (IGP). Therefore, the aerosol plume with high AOD and low

266   SSA (high absorbing) was significant. Except for the inland parts of India, AEH in

267   severe aerosol plumes ranged from 1.5 to 3.5 km, and AEH was stably estimated across

268   the entire observation period.

(a) TROPOMI ALH 2021/03/28   **(b)** TROPOMI ALH 2021/03/29
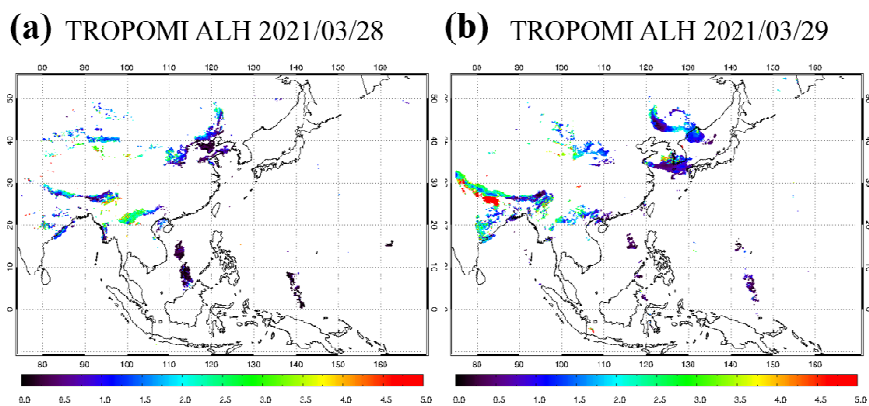
269

270   **Figure 3.** ALH retrieved from TROPOMI on (a) March 28 and (b) March 29, 2021.

271

272   For comparison of the retrieval, Figure 3 shows the ALH retrieved from TROPOMI

273   on March 28 and 29, 2021 over East Asia. A dust plume was transported from China to

274   South Korea during this period, then split into two distinct plumes over northeastern

275   China and the coastal area of South Korea. The ALH retrieved from TROPOMI for both

276   plumes were 0.5~1.5 km. The definition of ALH from TROPOMI is the optical centroid

277   layer height of the plume. Otherwise, the AEH product from GEMS is defined as the

Atmospheric
Measurement
Techniques
Discussions

Open Access

EGU

278   height with aerosol extinction integrated from the surface of $(1-\exp^{-1}) \times$ AOD. Given

279   this difference in definition for the aerosol height parameter, larger aerosol heights were

280   retrieved from GEMS compared to TROPOMI. In an ideal case, the AEH from GEMS

281   was overestimated by around 0.5 km relative to the ALH from TROPOMI, assuming the

282   aerosol vertical distribution was a Gaussian with a width of 1 km. Although AEH had

283   higher values than ALH from TROPOMI, the GEMS AEH retrievals for the dust

284   transport case study were good.

285   Furthermore, the retrieval area covered by GEMS is larger than by TROPOMI, as

286   demonstrated by a comparison of Figures 2 and 3. In East Asia, AEH from GEMS

287   estimated a continuous dust plume from China to South Korea. In addition, the GEMS

288   retrieval results estimated greater aerosol height information in coastal India compared

289   to TROPOMI. Although high height values were retrieved for clear-sky regions, in

290   particular low latitude ocean regions, the AEH from GEMS was successfully retrieved

291   over the area of interest for the case study.

292

Atmospheric
Measurement
Techniques
Discussions
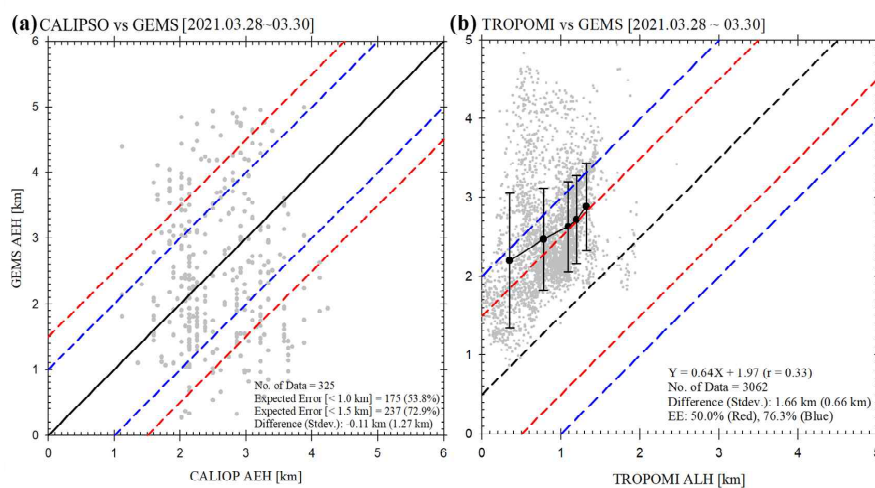
Figure 4. Intercomparison of (a) AEH between CALIOP and GEMS and (b) ALH from TROPOMI and AEH from GEMS over the period from March 28 to 30, 2021.
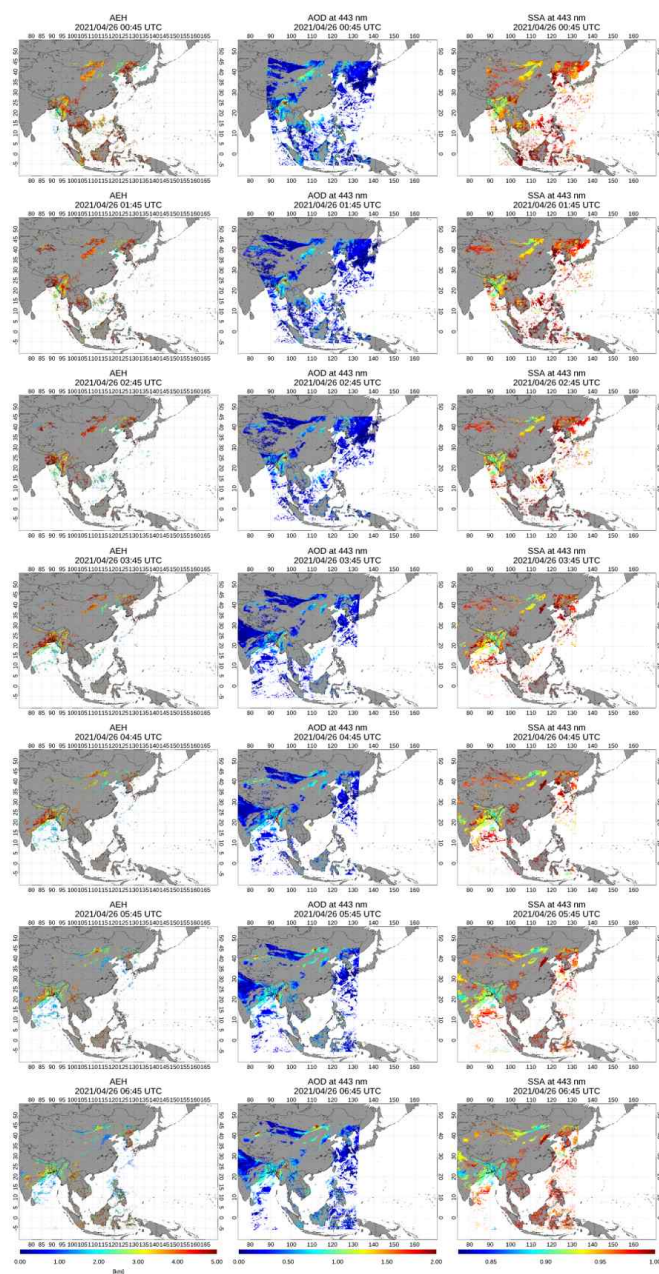
Figure 4 shows intercomparison results for aerosol plume height among GEMS, CALIOP, and TROPOMI during the case study of Yellow dust transport in East Asia from March 28 to 30, 2021. For spatial colocation, we selected pixels for which distance between GEMS and CALIOP observations was less than 50 km. In addition, only the closest 10% of pixels were used. Given the different orbital characteristics of CALIOP and GEMS, temporal colocation was also considered. During the period of image scanning from east to west over Asia by GEMS, CALIOP passes through the GEMS observation area from south to north every 98.3 minutes. On average, CALIOP passes three to four orbits through the GEMS scan area during a single day of daytime observation. To consider these different orbital characteristics, temporal colocation was limited to a 1-hour difference between CALIOP and GEMS scans. As GEMS observes hourly, colocated pixels between the two satellites shift from east to west over time.

309 Ultimately, the number of colocated pixels with AOD at 443 nm > 0.3 was 534 for this

310 case study.

311 For the direct comparison shown in Figure 4a, the difference in AEH between GEMS

312 and CALIOP was -0.11±1.27 km. Nanda *et al.* (2020) reported that the difference in

313 ALH between TROPOMI and CALIOP was 0.53 km for 4 cases of thick Saharan dust

314 plumes. In addition, 53.8% and 72.9% of the total pixels showed differences less than

315 1.0 and 1.5 km, respectively. Large AEH uncertainty occurred mostly over the inland

316 area of China. Because AEH from GEMS uses only the O_2-O_2 absorption band, the

317 accuracy of AEH is sensitive to uncertainty in surface reflectance and AOD. Although

318 GEMS accurately estimated surface reflectance in near real time, this study used the

319 minimum reflectance under the Lambertian assumption to retrieve AOD and AEH. For

320 this reason, the retrieved results were significantly affected by uncertainty in surface

321 properties during the observation period.

322 Figure 4b shows a comparison of GEMS and TROPOMI for the period of March 28

323 ~ 30, 2021 in East Asia. To ensure the accuracy of ALH from TROPOMI, only pixels

324 with quality assurance (QA) values greater than 0.5 were used. The difference between

325 GEMS AEH and TROPOMI ALH was 1.66 ± 0.66 km in this case, and 49.9% of all

326 pixels had differences less than 1.5 km. This proportion value was lower than the

327 corresponding result from the comparison of GEMS and CALIOP. However, the ALH

328 from TROPOMI is generally lower than the AEH from GEMS because of the

329 discrepancy in definitions. To correct the inconsistency of definition, the difference

330 between two retrieval results decreased to 0.5 km bias. After correction, 50.0% and

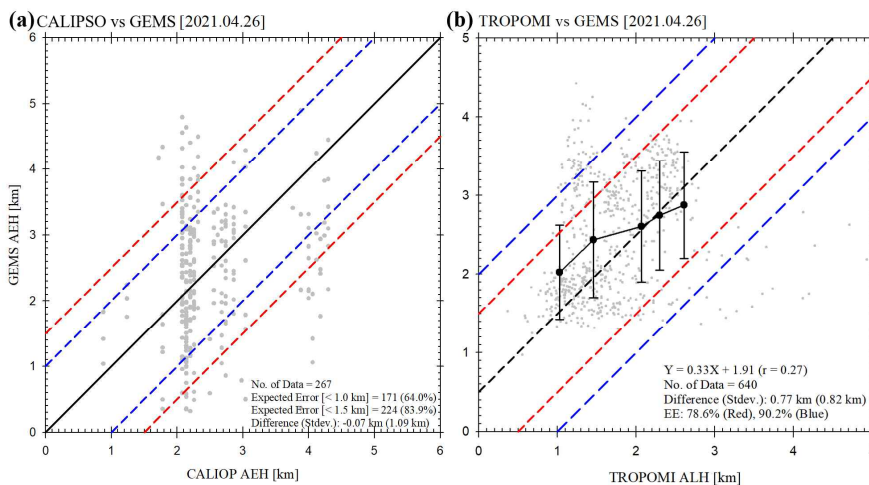331 76.3% of pixels are within the expected error ranges of 1.0 and 1.5 km, respectively.

Figure 5. Case study results for AEH, AOD, and SSA based on GEMS observations on April 26, 2021.
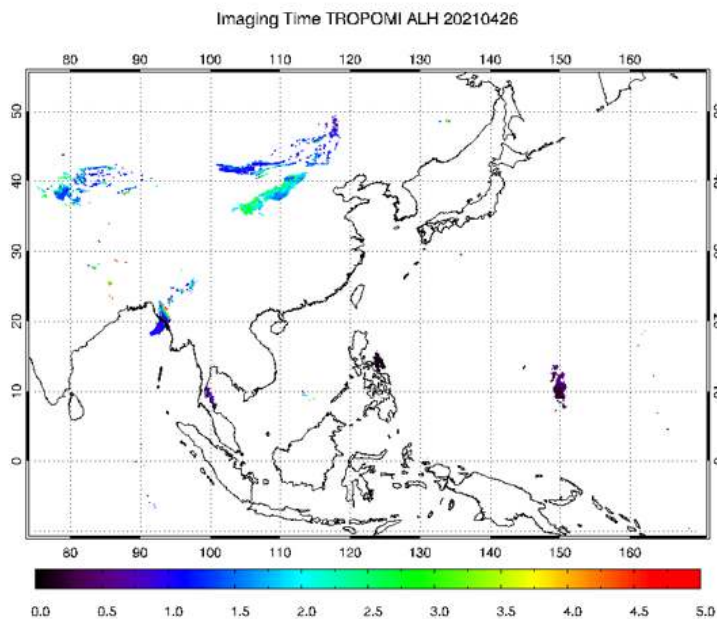
Figure 6. ALH retrieved from TROPOMI on April 26, 2021.

Figure 7. Intercomparison of (a) AEH between CALIOP and GEMS, and (b) ALH from

TROPOMI and AEH from GEMS on April 26, 2021.

Atmospheric
Measurement
Techniques
Discussions

Open Access

EGU

341   An additional intercomparison case of April 26, 2021 is shown in Figures 5 (GEMS)

342   and 6 (TROPOMI). During the transport of the Yellow dust plume from inland China to

343   the coastal area, AEH changed from 4.0 km at 02:00 UTC to 2.0 km at 06:00 UTC. By

344   contrast, ALH from TROPOMI only observed the 1.5~2.5 km layer height over East

345   Asia around 04:00 UTC. Although the AEH from GEMS had spatio-temporal

346   uncertainty, this case demonstrates the advantage of AEH retrieval from GEMS for

347   continuous monitoring of changes in plume height, in particular during dust transport.

348   As shown in Figure 7, AEH from GEMS showed differences in height of -0.07 ± 1.09

349   km (compared to CALIOP) and 0.77 ± 0.82 km (compared to TROPOMI). These

350   comparison results show that the GEMS algorithm accurately retrieved AEH and can be

351   used in several application studies.

352

353   **5. Long-term validation**

354   For long-term validation, we used the AEH retrieval results from January to June,

355   2021. Similar to the case studies, intercomparison datasets from CALIOP and

356   TROPOMI were selected containing mean layer height values in the closest 10% of

357   pixels within a 50 km range for spatial colocation. In addition, only observations taken

358   within ±1 hour of the GEMS observation time were selected for temporal colocation. As

359   the CALIOP and TROPOMI satellites passed over the study area around 13:30 local

360   time, which is around 04:30 UTC for East Asia and around 06:30 UTC for India. Most

361   temporal colocation pixels aligned with observation times of 04:00~06:00 UTC,

362   respectively. To check the dependence of several retrieval variables, the AI value for UV

363   (UVAI), AOD, SSA, and dominant aerosol type in each pixel (TYPE) were obtained

364   from the L2AERAOD. Although the GEMS algorithm retrieved AEH in the range of

365 0~10 km, the sensitivity of O_2-O_2 SCD was weak in cases of high AEH because of the

366 vertical distribution of air molecules. To ensure sufficient quality of retrieved data,

367 therefore, the AEHs from GEMS and CALIOP, and the ALH from TROPOMI were

368 used only in pixels where the AEH from GEMS were lower than 5 km.
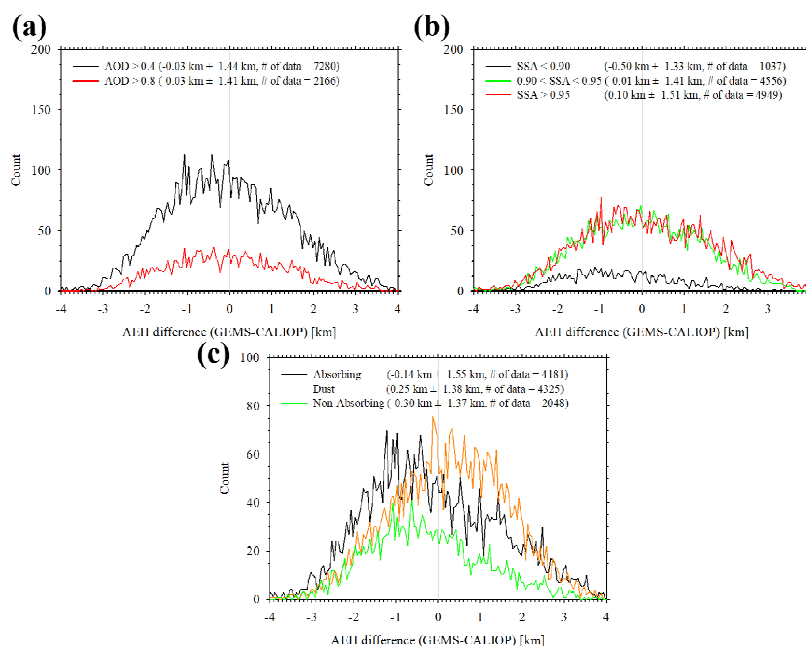
369

370 **Figure 8.** Histogram of AEH difference between CALIOP and GEMS with respect to

371 (a) AOD, (b) SSA, and (c) TYPE from GEMS over the period from January 1 to June

372 30, 2021.

373

374 Figure 8 shows histograms of difference in AEH between GEMS and CALIOP

375 according to AOD at 443 nm, SSA at 443 nm, and TYPE from GEMS. From Figure 8a,

376 the dependence on AOD threshold was insignificant; the average estimated AEH

377 difference was -0.03 km, but the variation in AEH difference was around 1.4 km based

378   on the standard deviation for AOD > 0.4. Because of uncertainty in GEMS operational

379   products, AEH from GEMS exhibits large variability. As reported by Park *et al.* (2016),

380   error budgets of AEH from O_2-O_2 SCD were 105~387, 72~352, and 576~1047 m

381   because of uncertainty in AOD, aerosol particle size, and SSA, respectively. Although

382   L2AERAOD accurately retrieved the optical and physical properties of aerosols (AOD,

383   SSA, and TYPE), the retrieved results still remained significant uncertainty. Go *et al.*

384   (2020) noted that the UV aerosol retrieval algorithm, which is the basic method to the

385   L2AERAOD algorithm, has significant root mean square errors (RMSEs) for both AOD

386   and SSA compared to ground-based data. Combined with the high sensitivity of AEH

387   errors to aerosol optical properties, uncertainty arising from L2AERAOD causes

388   significant variability in AEH.

389   Additional potential sources of error for AEH from GEMS are uncertainty in surface

390   reflectance and the discrepancy in O_2-O_2 SCD values between the simulation results and

391   observations. Park *et al.* (2016) found that O_2-O_2 SCD significantly alters the surface

392   reflectance and is an error source affecting AEH retrieval. Although the fitting error of

393   O_2-O_2 SCD from GEMS radiance was minimized, the fitting error is still remained

394   around 6%, as indicated in Table 2. Significant fitting error perturbs the fitting signals

395   and tends to result in the underestimation of SCD. The discrepancy in fitting condition

396   between the simulated and observed radiance biased the SCD estimation, which in turn

397   led to bias and variation in the AEH retrieval.

398   The variation in AEH difference between observation platforms is shown in Figure 8b

399   as a histogram according to SSA threshold. Across the entire SSA threshold range, the

400   standard deviation of the AEH difference was 1.33~1.51 km. In particular, this standard

401   deviation decreased slightly with decreasing SSA. Aerosol height information is

402   significantly more sensitive to absorbing-dominant aerosols than scattering-dominant

403   aerosols (e.g., Park *et al.*, 2016; Nanda *et al.*, 2020). Even if the uncertainty due to

404   aerosol properties is fixed, the variability of AEH is affected by the sensitivity of AEH

405   error to aerosol absorptivity.

406   Figure 8c shows the dependence of AEH difference on TYPE. Changing the Type

407   significantly changed the mean value of AEH difference. The TYPE product included

408   dependence on the aerosol size and optical absorptivity. For this reason, the AEH

409   difference graphs for the "Dust" and "Absorbing" types differ, despite both types being

410   absorbing-dominant aerosols. The AEH difference for the "Absorbing" type showed a

411   negative bias with a large standard deviation, whereas a positive bias with a small

412   standard deviation was obtained for the "Dust" type. The AEH difference for the "Non-

413   Absorbing" aerosol type showed the largest negative bias in this comparison. These

414   results suggest that the aerosol size distribution of fine particles affects the negative bias

415   of AEH. Combined with the AEH difference bias illustrated in Figure 8b, these findings

416   indicate that the bias in AEH difference for "Absorbing" aerosols is weakened by their

417   absorbing-dominant property.

418   Figure 9 shows means and standard deviations for AEH difference between CALIOP

419   and GEMS according to AOD and AI values from GEMS. For AOD, the mean AEH

420   difference ranged from -0.13 to 0.03 km with a standard deviation of approximately

421   1.45 km. Similar to Figure 8a, the variation in AEH difference with AOD change was

422   insignificant. For AI, the smallest AEH difference was -0.19 km, obtained for the AI

423   range of 1.5~2.0. The largest AEH difference was 0.24 km for the AI range of 4.0~4.5.

424   Although the AEH difference varied slightly, no consistent tendency in AEH variation

425   with AI was observed Overall, the standard deviation of AEH difference ranged from

426   1.49 km (0.0 < AI < 0.5) to 1.18 km (4.5 < AI < 5.0), and a consistent tendency of

427   decreasing variance in AEH difference was found with increasing AI.

(a)

(b)
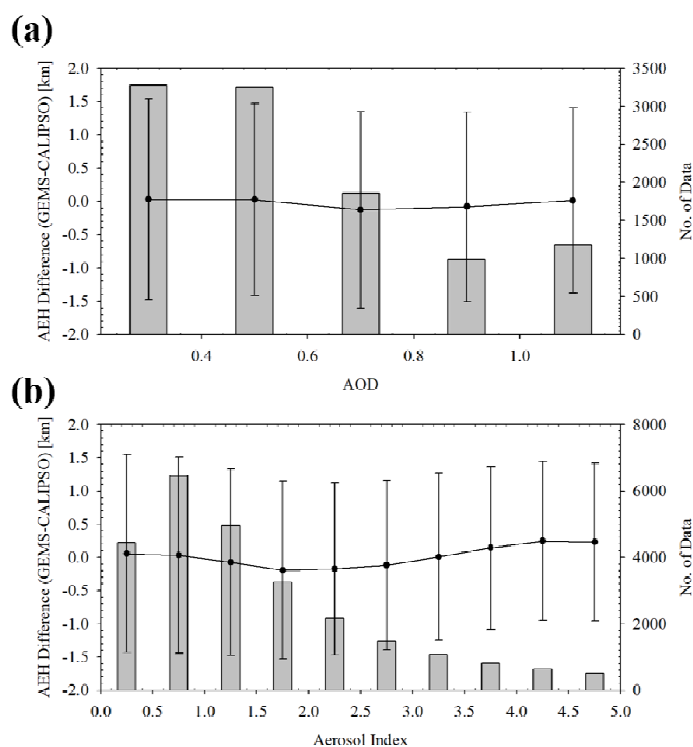
428

429   **Figure 9.** AEH difference between CALIOP and GEMS with respect to ranges of (a)

430   AOD and (b) AI obtained from GEMS from January 1 to June 30, 2021.

431

432   Figure 10 shows histograms of differences between ALH from TROPOMI and AEH

433   from GEMS [(AEH from GEMS) – (ALH from TROPOMI)] according to the SSA and

434   TYPE obtained from GEMS. As TROPOMI retrieved only ALH data with high QA

435   values over pixels containing strong aerosol plumes, the AOD dependence of aerosol

436   height difference is not shown in this comparison. In addition, the number of pixels

437   corresponding to scattering dominant aerosols (i.e., pixels with SSA > 0.95 or "Non-

438   Absorbing" type) was insufficient. Nanda *et al.* (2020) showed that the operational

439   algorithm of TROPOMI is limited to retrieving the ALH over scattering-dominant

440   aerosols. In addition, Griffin *et al.* (2020) reported that the small absorbing AI pixels are

441   identified with small QA values in the offline product of ALH.


442
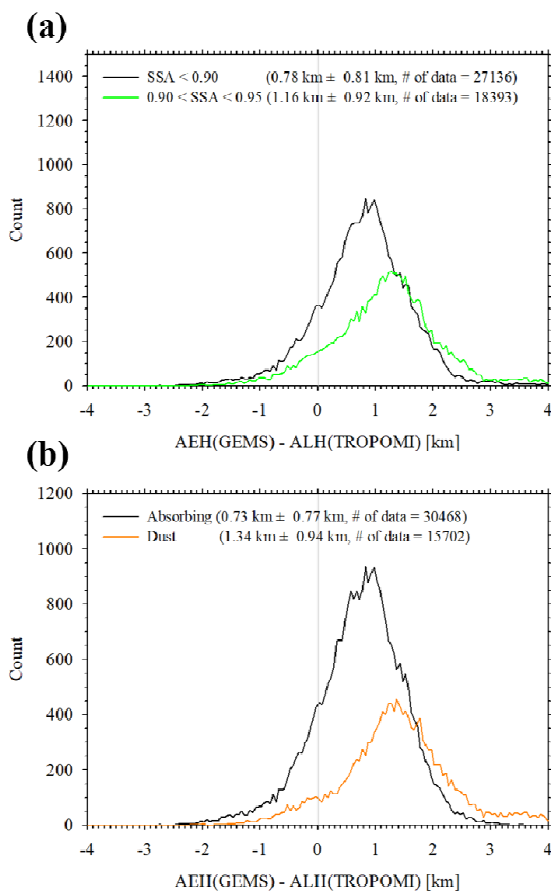
Figure 10. Histograms of differences between ALH from TROPOMI and AEH from
GEMS [(AEH from GEMS) – (ALH from TROPOMI)] with respect to (a) SSA, and (b)
TYPE from GEMS in the period from January 1 to June 30, 2021.

446   As shown in Figure 10, (AEH from GEMS) – (ALH from TROPOMI) was

447   significantly dependent on both SSA and TYPE. The mean value of (AEH from GEMS)

448   – (ALH from TROPOMI) decreased as the aerosol absorptivity increased. This

449   difference was 0.78 ± 0.81 and 1.16 ± 0.92 km for pixels of SSA < 0.90 and 0.90 < SSA

450   < 0.95, respectively. Comparing these results to Figure 8b, we find that the standard

451   deviation of the comparison with TROPOMI was approximately 60% of the

452   corresponding value for CALIOP. This smaller variability compared to CALIOP

453   appears to have arisen because both TROPOMI and GEMS are passive sensors that use

454   similar retrieval methods for oxygen-related absorption bands.

455   In addition, (AEH from GEMS) – (ALH from TROPOMI) was significantly

456   dependent on TYPE, as shown in Figure 10b. The difference was 0.73 ± 0.77 and $1.34 \pm$

457   0.94 km for "Absorbing" and "Dust" type aerosols, respectively. Similar to Figure 8c,

458   the TYPE dependence of aerosol height information was influenced by both

459   absorptivity and size information. In addition, the difference in the definition of ALH

460   from TROPOMI and AEH from GEMS impacted the comparison. "Dust" types of

461   aerosol are mainly transported in the free troposphere, and the associated plume

462   thickness is highly variable. By contrast, "Absorbing" aerosols mainly originate from

463   anthropogenic emissions in East Asia (e.g., Gao *et al.*, 2014; Wang *et al.*, 2012; Peng *et*

464   *al.*, 2016). In addition, the vertical distribution of aerosols is unstable for "Dust" case.

465   For these reasons, the standard deviation of aerosol height was larger for the "Dust"

466   type.
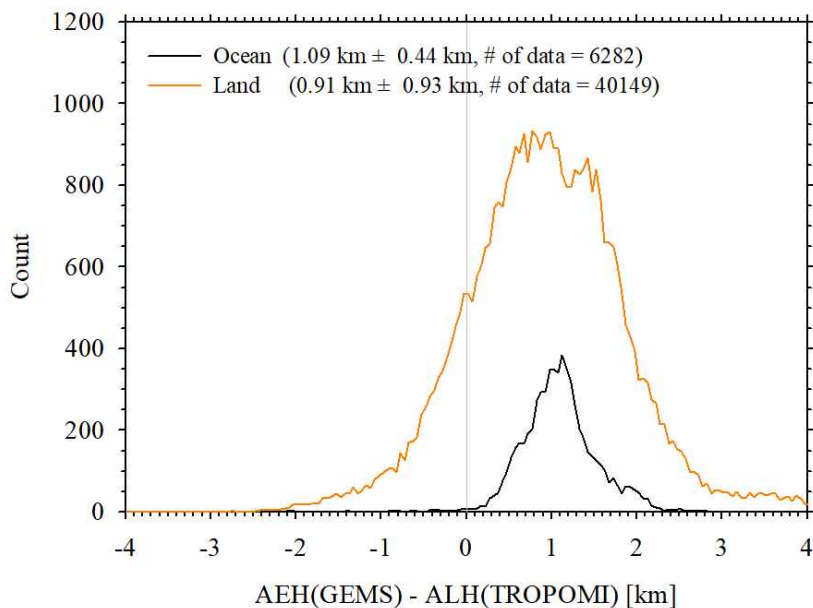
Figure 11. Histogram of the difference between ALH from TROPOMI and AEH
from GEMS [(AEH from GEMS) – (ALH from TROPOMI)] over land and ocean pixels,
respectively, from January 1 to June 30, 2021.

The non-Lambertian effect on the land surface impacted surface albedo uncertainty
during AEH retrieval, and this effect led to bias and variance in AEH. In this study, the
minimum Lambertian equivalent reflectance was used as the reference reflectance value.
However, surface reflectivity has geometric dependence due to non-Lambertian effects,
which leads to a bias of 0.01-0.02 for surface reflectance over the land surface (e.g., Qin
et al., 2019). To identify the sensitivity of surface property, a histogram was constructed
of (AEH from GEMS) – (ALH from TROPOMI) after classification into land and ocean
surface types, as shown in Figure 11. From the statistical results, the mean differences

480   were estimated to be 1.09 and 0.91 km for ocean and land pixels, respectively,

481   indicating insignificant difference in bias between these two surface covers. However,

482   the standard deviation of the two surface types indicated a significant difference. Over

483   the ocean surface, the histogram is very narrow. Although there are 6.5 times more data

484   for land than those for the ocean surface, the land surface has a relatively wide

485   histogram distribution. This discrepancy arises because the non-Lambertian effect

486   causes bias in surface reflectance, while also influencing the variability in surface

487   reflectance related to observation geometry. For this reason, land surface reflectance

488   based on the non-Lambertian surface assumption is not fully representative of actual

489   surface reflectance as a function of observation geometry. Therefore, the standard

490   deviation of the layer height difference is larger over the land surface, and the

491   significant difference between land and ocean pixels is mainly driven by the assumption

492   of surface reflection properties.
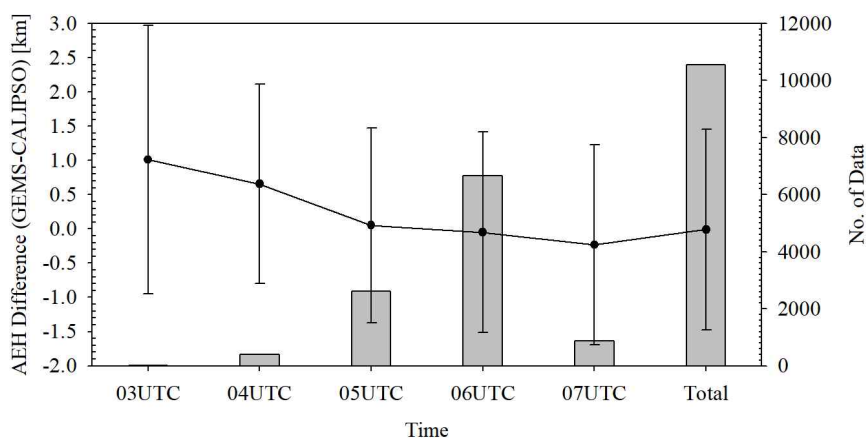
493

494   **Figure 12.** Diurnal dependence of AEH difference between CALIOP and GEMS

495   from January 1 to June 30, 2021.

Atmospheric
Measurement
Techniques
Discussions
Open Access

EGU

496

497   The results of hourly statistical analyses are presented in Figure 12. Because they use

498   a consistent definition of AEH, we show only a comparison of GEMS and CALIOP. The

499   diurnal variation in AEH difference ranged from -0.23 ± 1.45 km (07:00 UTC, Number

500   of Data = 867) to 1.01 ± 1.96 km (03:00 UTC, Number of Data = 23). However, the

501   number of pixels observed at 03:00 UTC was insufficient for the identification of

502   diurnal variation. The AEH difference of 0.66 ± 1.45 km was the next highest value

503   obtained at 04:00 UTC (Number of Data = 395). The inhomogeneous number of data is

504   mainly due to the lack of spatial homogeneity among retrieval pixels. Over India, very

505   high AOD values were consistently observed during the comparison period. Otherwise,

506   the AEH was only retrieved under conditions of severe anthropogenic emissions over

507   East Asia. In addition, the diurnal variation in AEH difference was caused by spatial

508   characteristics of AEH difference. From 03:00 to 05:00 UTC, CALIOP mainly passed

509   over East Asia, which has numerous sources of aerosol emissions, including biomass

510   burning, dust, and industrial activity. In addition, GEMS observed only the eastern part

511   of India, which is dominated by anthropogenic aerosols. The spatial distribution of the

512   dominant aerosol types may impact the diurnal variation in AEH difference.

513

514   **6. Summary & Conclusions**

515   Based on the possibility of retrieving AEH from environmental satellite sensors, an

516   AEH retrieval algorithm for GEMS was developed that solely uses the O_2-O_2 absorption

517   band with considering aerosol and surface properties. Because the sensitivity of AEH

518   retrieval is strongly affected by optical amounts and properties of aerosols, as well as

519   surface reflectivity, an AEH retrieval algorithm for GEMS was developed after retrieval

Atmospheric
Measurement
Techniques
Open Access

EGU

Discussions

520   of the GEMS operational algorithms, L2AERAOD and L2SFC. With the newly

521   developed retrieval algorithm, GEMS can be used to monitor aerosol vertical

522   information with high temporal and spatial resolution. To ensure significant sensitivity

523   of AEH retrieval, only AEH retrieval results are with AOD larger than 0.3 were shown.

524   For dust plumes over East Asia, AEH indicated significant aerosol vertical

525   information and insignificant diurnal variation in regions with severe dust plumes. After

526   spatial and temporal colocation, the AEH from GEMS aligned well with the AEH

527   information obtained from CALIOP. The differences in AEH between GEMS and

528   CALIOP for dust plume cases were -0.07 ± 1.09 and -0.11 ± 1.27 km, with 53.8% and

529   72.9% of all pixels showing differences less than 1.0 and 1.5 km, respectively. Large

530   AEH uncertainty was found mostly over inland China due to uncertainty in surface

531   reflectance and AOD over the land surface. In addition, AEH from GEMS was

532   overestimated compared to the TROPOMI ALH results due to different definitions of

533   ALH from TROPOMI and AEH from GEMS.

534   In long-term intercomparison with CALIOP, the average AEH difference was

535   estimated to be -0.03 km, with variation of around 1.4 km based on the standard

536   deviation for AOD > 0.4. In terms of sensitivity to surface albedo, the mean differences

537   were estimated to be 1.09 and 0.91 km over the ocean and land, respectively, which is

538   an insignificant difference of the biases between these two surface types. The large

539   variation in AEH difference between GEMS and CALIOP was caused by uncertainty in

540   the input parameters estimated from L2AERAOD and L2SFC. In the long-term

541   intercomparison with TROPOMI, this difference was significantly dependent on both

542   SSA and TYPE. The difference was 0.78 ± 0.81 km and 1.16 ± 0.92 km for pixels with

543   SSA < 0.90 and 0.90 < SSA < 0.95, respectively. In addition, differences of 0.73 ± 0.77

544   and 1.34 ± 0.94 km were obtained for the "Absorbing" and the "Dust" types of aerosol,

545   respectively. The AEH difference ranged from -0.23 ± 1.45 km (07:00 UTC, Number of

546   Data = 867) to 1.01 ± 1.96 km (03:00 UTC, Number of Data = 23), showing diurnal

547   dependence. The spatial difference in dominant aerosol type may impact the diurnal

548   variation in AEH difference.

549   The case studies and results of the long-term validation show that AEH retrieved

550   from GEMS can provide information on aerosol vertical distribution, with applications

551   in diverse research fields. In particular, AEH information can be applied to AMF

552   calculation for trace gases to consider the change in scattering weight change due to the

553   presence of an aerosol layer. In addition, AEH considerably affects the surface

554   particulate matter (PM) concentration obtained from satellite-based AOD because PM

555   estimation is significantly affected by the mixing layer height of aerosols. Although

556   several fields of study may apply the AEH retrieval results, uncertainty in AEH remains,

557   driving large deviations in some pixels. Moreover, AEH provides representative layer

558   height information as only one variable because of its sole reliance on O_2-O_2 SCD for

559   direct estimation of aerosol height information. This method is limited to the

560   consideration of aerosol vertical structures (i.e., Gaussian or exponential vertical

561   distribution structures). Rather than using the GEMS sensor alone, using another

562   absorption band for oxygen-based materials would provide additional scattering

563   information about aerosols.

564

565   **Acknowledgements**

568

Atmospheric
Measurement
Techniques
Discussions

569 **References**

570 Accarreta, J. R., de Haan, J. F., and Stammes, P.: Cloud pressure retrieval using the O2-
571   O2 absorption band at 477 nm, J. Geophys. Res., 109, D05204,
572   doi:10.1029/2003JD003915, 2004

573 Ahn, C., Torres, O., and Jethva, H.: Assessment of OMI near-UV aerosol optical depth
574   over land, J. Geophys. Res., 119, 2457-2473, 2014.

575 Bogumil, K., Orphal, J., Burrows, J. P., and Flaud, J. M.: Vibrational progressions in the
576   visible and near-ultraviolet absorption spectrum of ozone, Chem. Phys. Lett., 349,
577   241-248, 2001.

578 Buchard, V., de Silva, A. M., Colarco, P. R., Darmenov, A., Randles, C. A., Govindaraju,
579   R., Torres, O., Campbell, J., and Spurr, R.: Using the OMI aerosol index and
580   absorption aerosol optical depth to evaluate the NASA MERRA Aerosol reanalysis,
581   Atmos. Chem. Phys., 15, 5743-5760, 2015.

582 Chen, X., Wang, J., Xu, X., Zhou, M., Zhang, H., Garcia, L. C., Colarco, P. R., Janz, S.
583   J., Yorks, J., McGill, M., Reid, J. S., de Graaf, M., and Kondragunta, S.: First
584   retrieval of absorbing aerosol height over dark target using TROPOMI oxygen B
585   band: Algorithm development and application for surface particulate matter
586   estimates, Remote Sens. Env., 265, 112674, 2021.

587 Chimot, J., Veefkind, J. P., Vlemmix, T., de Haan, J. F., Amiridis, V., Proestakis, E.,
588   Marinou, E., and Levelt, P. F.: An exploratory study on the aerosol height retrieval
589   from OMI measurements of the 477 nm O2-O2 spectral band using a neural
590   network approach, Atmos. Meas. Tech., 10, 783-809, 2017.

591 Choi, H., Liu, X., Abad, G. G., Seo, J., Lee, K. -M., and Kim, J.: A fast retrieval of cloud
592   parameters using a Triplet of wavelengths of oxygen dimer band around 477 nm,
593   Remote Sens., 13, 152, doi: 10.3390/rs13010152, 2021.

594 Choi, W., Lee, H., Kim, J., Ryu, J. -Y., Park, S. S., Park, J., and Kang, H.: Effects of
595   spatiotemporal O4 column densities and temperature-dependent O4 absorption
596   cross-section on an aerosol effective height retrieval algorithm using the O4 air
597   mass factor from the ozone monitoring instrument, Remote Sens. Env., 229, 223-
598   233, 2019.

599   Choi, W., Lee, H., and Kim, J.: First TROPOMI retrieval of aerosol effective height
600   using O4 absorption band at 477 nm and aerosol classification, IEEE Trans.
601   Geosci., Remote Sens., 59, 9873-9886, 2021.

602   de Graaf, M., Stammes, P., Torres, O., and Koelemeijer, R. B. A.: Absorbing aerosol
603   index: Sensitivity analysis, application to GOME and comparison with TOMS, J.
604   Geophys. Res., 110, D01201, doi:10.1029/2004JD005178, 2005.

605   de Graaf, M., de Haan, J. F., and Sanders, A. F. J.: TROPOMI ATBD of the Aerosol
606   Layer Height, 75pp, Royal Netherlands Meteorological Institute, Netherland.

607   Ding, S., Wang, J., and Xu, X.: Polarimetric remote sensing in oxygen A and B bands:
608   Sensitivity study and information content analysis for vertical profile of aerosols,
609   Atmos. Meas. Tech, 9, 2077-2092, 2016.

610   Dubuisson, P., Frouin, R., Dessaily, D., Duforet, L., Leon, J. –F., Voss, K., and Antoine,
611   D.: Estimating the altitude of aerosol plumes over the ocean from reflectance ratio
612   measurements in the O2 A-band, Remote Sens. Environ., 113, 1899-1911,
613   doi:10.1016/j.rse.2009.04.018, 2009.

614   Gao, Y., Zhao, C., Liu, X., Zhang, M., and Leung, L. R.: WRF-Chem simulations of
615   aerosols and anthropogenic aerosol radiative forcing in East Asia, Atmos. Environ.,
616   92, 250-266, 2014.

617   Geddes, A., and Boesch, H.: Tropospheric aerosol profile information from high-
618   resolution oxygen A-band measurements from space, Atmos. Meas. Tech., 8, 859-
619   874, 2015.

620   Go, S., Kim, J., Park, S. S., Kim, M., Lim, H., Kim, J. -Y., Lee, D. -W., and Im, J.:
621   Synergistic use of hyperspectral UV-visible OMI and broadband meteorological
622   imager MODIS data for a merged aerosol product, Remote Sens., 12, 3987,
623   doi:10.3390/rs12233987, 2020.

624   Griffin, D., Sioris, C., Chen, J., Dickson, N., Kovachik, A., de Graaf, M., Nanda, S.,
625   Veefkind, P., Dammers, E., McLinden, C. A., Makar, P., and Akingunola, A.: The
626   2018 fire season in North America as seen by TROPOMI: aerosol layer height
627   intercomparisons and evaluation of model-derived plume heights, Atmos. Meas.
628   Tech., 13, 1427-1445, 2020.

Atmospheric
Measurement
Techniques
Discussions

Open Access

629 Herman, J. R., Bhartia, P. K., Torres, O., Hsu, C., Seftor, C., and Celarier, E.: Global

630   distribution of UV-absorbing aerosols from Nimbus-7/TOMS data, J. Geophys.

631   Res., 102(D14), 16911-16922, 1997.

632 Hong, H., Lee, H., Kim, J., Jeong, U., Ryu, J., and Lee, D. S.: Investigation of

633   simultaneous effects of aerosol properties and aerosol peak height on the air mass

634   factors for space-borne NO2 retrievals, Remote Sens., 9, 208,

635   doi:10.3390/rs9030208, 2017.

636 Joiner, J., and Bhartia, P. K.: The determination of cloud pressures from rotational

637   Raman scattering in satellite backscatter ultraviolet measurements, J. Geophys.

638   Res., 100, 23019-23026, 1995.

639 Joiner, J., and Vasilkov, A. P.: First results from the OMI rotational Raman scattering

640   cloud pressure algorithm, IEEE Trans. Geosci. Remote Sens., 44, 1272-1282, 2006.

641 Kim, M., Kim, J., Torres, O., Ahn, C., Kim, W., Jeong, U., Go, S., Liu, X., Moon, K. J.,

642   and Kim D. -R.: Optimal estimation-based algorithm to retrieve aerosol optical

643   properties for GEMS measurements over Asia, 10, 162, doi:10.3390/rs10020162,

644   2018.

645 Kim, J., Jeong, U., Ahn, M. -H., Kim, J. H., Park, R. J., Lee, H., Song, C. H., Choi, Y. -

646   S., Lee, K. -H., Yoo, J. -M., Jeong, M. -J., Park, S. K., Lee, K. -M., Song, C. -K.,

647   Kim, S. -W., Kim, Y. J., Kim, S. -W., Kim, M., Go, S., Liu, X., Chance, K., Chan

648   Miller, C., Al-Saadi, J., Veihelmann, B., Bhartia, P. K., Torres, O., González Abad,

649   G., Haffner, D. P., Ko, D. H., Lee, S. H., Woo, J. -H., Chong, H., Park, S. S., Nicks,

650   D., Choi, W. J., Moon, K. -J., Cho, A., Yoon, J., Kim, S. -K., Hong, H., Lee, K.,

651   Lee, H., Lee, S., Choi, M., Veefkind, P., Levelt, P. F., Edwards, D. P., Kang, M., Eo,

652   M., Bak, J., Baek, K., Kwon, H. -A., Yang, J., Park, J., Han, K. M., Kim, B. -R.,

653   Shin, H. -W., Choi, H., Lee, E., Chong, J., Cha, Y., Koo, J. -H., Irie, H., Hayashida,

654   S., Kasai, Y., Kanaya, Y., Liu, C., Lin, J., Crawford, J. H., Carmichael, G. R.,

655   Newchurch, M. J., Lefer, B. L., Herman, J. R., Swap, R. J., Lau, A. K. H., Kurosu,

656   T. P., Jaross, G., Ahlers, B., Dobber, M., McElroy, C. T., and Choi, Y.: New era of

657   air quality from Space: Geostationary Environment Monitoring Spectrometer

658   (GEMS), Bul. Ame. Meteorol. Soc., 101(1), E1−E22, 2020.

Atmospheric
Measurement
Techniques
Discussions

659 Kokhanovsky, A. A., and Rozanov, V. V.: The determination of dust cloud altitudes from
660   a satellite using hyperspectral measurements in the gaseous absorption band, Int. J.
661   Rem. Sens., 31, Nos. 9-10, 2729-2744, 2010.

662 Kooreman, M. L., Stammes, P., Trees, V., Sneep, M., Tilstra, L. G., de Graaf, M.,
663   Zweers, D. C. S., Wang, P., Tuinder, O. N. E., and Veefkind, J. P.: Effects of cloud
664   on the UV absorbing aerosol index from TROPOMI, Atmos. Meas. Tech., 13,
665   6407-6426, 2020.

666 Lorente, A., Boersma, K. F., Yu, H., Doerner, S., Hilboll, A., Richter, A., Liu, M.,
667   Lamsal, L. N., Barkley, M., De Smedt, I., Van Roozendael, M., Wang, Y., Wagner,
668   T., Beirle, S., Liu, J. -T., Krotkov, N., Stammes, P., Wang, P., Eskes, H. J., and Krol,
669   M.: Structural uncertainty in air mass factor calculation for NO2 and HCHO
670   satellite retrieval, Atmos. Meas. Tech., 10, 759-782, 2017.

671 Nanda, S., de Graaf, M., Sneep, M., de Haan, J. F., Stammes, P., Sanders, A. F. J.,
672   Tuinder, O., Veefkind, J. P., and Levelt, P. F.: Error sources in the retrieval of
673   aerosol information over bright surfaces from satellite measurements in the oxygen
674   A band, Atmos. Meas. Tech., 11, 161–175, https://doi.org/10.5194/amt-11-161-
675   2018, 2018.

676 Nanda, S., de Graaf, M., Veefkind, J. P., Sneep, M., ter Linden, M., Sun, J., and Level, P.
677   F.: A first comparison of TROPOMI aerosol layer height (ALH) to CALIOP data,
678   Atmos. Meas. Tech., 13, 3043-3059, 2020.

679 National Institute of Environmental Research, Geostationary Environment Monitoring
680   Spectrometer (GEMS) Algorithm Theoretical Basis Document: Aerosol Retrieval
681   Algorithm, 42pp, Ministry of Environment, Korea, 2020a.

682 National Institute of Environmental Research, Geostationary Environment Monitoring
683   Spectrometer (GEMS) Algorithm Theoretical Basis Document: Surface
684   Reflectance Algorithm, 35pp, Ministry of Environment, Korea, 2020b.

685 Park, S. S., Kim, J., Lee, H., Torres, O., Lee, K. –M., and Lee, S. D.: Utilization of O4
686   slant column density to derive aerosol layer height from a space-borne UV-visible
687   hyperspectral sensor: Sensitivity and case study, Atmos. Chem. Phys., 16, 1987-
688   2006, doi:10.5194/acp-16-1987-2016, 2016.

689   Park, S. S., Takemura, T., and Kim, J.: Effect of temperature-dependent cross sections
690   on O4 slant column density estimation by a space-borne UV-visible hyperspectral
691   sensor, Atmos. Environ., 152, 98-110, 2017.

692   Peng, J., Hu, M., Guo, S., Du, Z., Zheng, J., Shang, D., Zamora, M. L., Zeng, L., Shao,
693   M., Wu, Y. -S., Zheng, J., Wang, Y., Glen, C. R., Collins, D. R., Molina, M. J., and
694   Zhang R.: Markedly enhanced absorption and direct radiative forcing of black
695   carbon under polluted urban environments, Proc. Natl. Acad. Sci., 113, 4266-4271,
696   2016.

697   Penning de Vries, M. J. M., Beirle, S., and Wagner, T.: UV aerosol indices from
698   SCIAMACHY: Introducing the Scattering Index (SCI), Atmos. Chem. Phys., 9,
699   9555-9567, 2009.

700   Penning de Vries, M. J. M., Beirle, S., Hoermann, C., Kaiser, J. W., Stammes, P., Tilstra,
701   L. G, Tuinder, O. N. E., and Wagner, T.: A global aerosol classification algorithm
702   incorporating multiple satellite data sets of aerosol and trace gas abundances,
703   Atmos. Chem. Phys., 15, 10597-10618, 2015.

704   Prospero, J. M., Ginoux, P., Torres, O., Nicholson, S. E., and Gill T. E.: Environmental
705   characterization of global sources of atmospheric soil dust identified with the
706   Nimbus 7 total ozone mapping spectrometer (TOMS) absorbing aerosol product,
707   Rev. Geophys., 40, 1002, doi:10.1029/2000RG000095, 2002.

708   Qin, W., Fasnacht, Z., Haffner, D., Vasilkov, A., Joiner, J., Krotkov, N., Fisher, B., and
709   Spurr, R.: A geometry-dependent surface Lambertian-equivalent reflectivity
710   product for UV-vis retrievals – Part 1: Evaluation over land surfaces using
711   measurements from OMI at 466 nm, Atmos. Meas. Tech., 12, 3997-4017, 2019.

712   Rana, A., Jia, S., and Sarkar, S.: Black carbon aerosol in India: A comprehensive review
713   of current status and future prospects, Atmos. Res., 218, 207-230, 2019.

714   Sanders, A. F. J., de Haan, J. F., Sneep, M., Apituley, A., Stammes, P., Vieitez, M. O.,
715   Tilstra, L. G., Tuinder, O. N. E., Koning, C. E., and Veefkind, J. P.: Evaluation of
716   the operational Aerosol Layer Height retrieval algorithm for Sentinel-5 Precursor:
717   application to O2 A band observations from GOME-2A, Atmos. Meas. Tech., 8,
718   4947-4977, 2015.

719   Sanders, A. F. J. and de Haan, J. F.: TROPOMI ATBD of the Aerosol Layer Height
720   product, available at: http://www.tropomi.eu/sites/default/files/files/S5P-KNMI-

Atmospheric
Measurement
Techniques
Discussions

721   L2-0006-RP-TROPOMI_ATBD_Aerosol_Height-v1p0p0-20160129.pdf (last

722   access: 8 June 2020), 2016.

723 Sanghavi, S., Martonchik, J. V., Landgraf, J., and Platt, U.: Retrieval of optical depth

724   and vertical distribution of particulate scatterers in the atmosphere using O2 A- and

725   B-band SCIAMACHY observations over Kanpur: A case study, Atmos. Meas.

726   Tech., 5, 1099-1119, 2012.

727 Spurr, R. "User's Guide VLIDORT Version 2.6, RT Solutions.", Cambridge, MA,

728   USA, 2013.

729 Thalman, R., and Volkamer, R.: Temperature dependent absorption cross-sections of

730   O2-O2 collision pairs between 340 and 630 nm and at atmospherically relevant

731   pressure. Phys. Chem. Chem. Phys. 15, 15371e15381, 2013.

732 Torres, O., Bhartia, P. K., Herman, J. R., Ahmad, Z., and Gleason, J.: Derivation of

733   aerosol properties from satellite measurements of backscattered ultraviolet

734   radiation: Theoretical basis, J. Geophys. Res., 103(14), 17099-17110, 1998.

735 Torres, O., Decae, R., Veefkind, P., and de Leeuw, G.: OMI Aerosol Retrieval Algorithm,

736   OMI Algorithm Theoretical Basis Document, Vol. III, Clouds, Aerosols and

737   Surface UV Irradiance, NASA-KNMI ATBD-OMI-03, pp. 47-71, 2002.

738 Torres, O., Jethva, H., Ahn, C., Jaross, G., and Loyola, D. G.: TROPOMI aerosol

739   products: evaluation and observations of synoptic-scale carbonaceous aerosol

740   plumes during 2018-2020, Atmos. Meas. Tech., 13, 6789-6806, 2020.

741 Vandaele, A. C., Hermans, C., Simon, P. C., Carleer, M., Colin, R., Fally, S., Merienne,

742   M. F., Jenouvrier, A., and Coquart, B.: Measurements of the NO2 absorption cross-

743   section from 42000 cm-1 to 10000 cm-1 (238-1000 nm) at 220 K and 294 K, J.

744   Quant. Spectrosc. Radiat. Transfer, 59, 3-5, 171-184, 1998.

745 Vasilkov, A., Joiner, J., Spurr, R., Bhartia, P. K., Levelt, P., and Stephens, G.: Evaluation

746   of the OMI cloud pressures derived from rotational Raman scattering by

747   comparisons with other satellite data and radiative transfer simulations, J. Geophys.

748   Res., 113, D15S19, doi:10.1029/2007JD008689, 2008.

749 Vasilkov, A., Yang, E. -S., Marchenko, S., Qin, W., Lamsal, L., Joiner, J., Krotkov, N.,

750   Haffner, D., Bhartia, P. K., and Spurr, R.: A cloud algorithm based on the O2-O2

751   477 nm absorption band featuring an advanced spectral fitting method and the use

Atmospheric
Measurement
Techniques
Discussions

752   of surface geometry-dependent Lambertian-equivalent reflectivity, Atmos. Meas.

753   Tech., 11, 4093-4107, 2018.

754 Wang, R., Tao, S., Wang, W., Liu, J., Shen, H., Shen, G., Wang, B., Liu, X., Li, W.,

755   Huang, Y., Zhang, Y., Lu, Y., Chen, H., Chen, Y., Wang, C., Zhu, D., Wang, X., Li,

756   B., Liu, W., and M, J.: Black carbon emissions in China from 1949 to 2050,

757   Environ., Sci. Technol., 46, 7595-7603, 2012.

758 Winker, D. M., Vaughan, M. A., Omar, A. H., Hu, Y., Powell, K. A., Liu, Z., Hunt, W.

759   H., and Young, S. A.: Overview of the CALIPSO mission and CALIOP data

760   processing algorithms, J. Atmos. Oceanic Technol., 26, 2310-2323, 2009.

761 Zeng, Z. -C., Chen, S., Natraj, V., Le, T., Xu, F., Merrelli, A., Crisp, D., Sander, S. P.,

762   and Yung, Y. L.: Constraining the vertical distribution of coastal dust aerosol using

763   OCO-2 O2 A-band measurements, Remote Sens. Env., 236, 111494, 2020.

764